coatings

MDPI

Article

Self-Healing Phenomenon at the Cut Edge of Zn-Al-Mg Alloy Coated Steel in Chloride Environments

Sang-Hee Kim [1], Seo-Yun Jin [2], Ji-Hoon Yang [3], Jeong-Hyeon Yang [4], Myeong-Hoon Lee [5] and Yong-Sup Yun [1,*]

[1] Department of Coast Guard Studies, Korea Maritime and Ocean University, Busan 49112, Republic of Korea; bullnaby@g.kmou.ac.kr
[2] Sewon America, Inc., Lagrange, GA 30241, USA; seoyunjin@g.kmou.ac.kr
[3] Materials Performance Research Group, POSCO Steel Solution Research Lab., POSCO Global R&D Center, Incheon 21985, Republic of Korea; jihoonyang@posco.com
[4] Department of Mechanical System Engineering, Gyeongsang National University, Tongyeong 53064, Republic of Korea; jh.yagi@gnu.ac.kr
[5] Korea Institute of Corrosion Science and Technology, Korea Maritime and Ocean University, Busan 49112, Republic of Korea; leemh@kmou.ac.kr
* Correspondence: ysyun@kmou.ac.kr

Abstract: This study explores the self-healing phenomenon at the cut edges of Zn-Al-Mg alloy coated steel in chloride environments, a critical consideration for materials exposed to marine conditions. Zn-Al-Mg coatings offer superior resistance to cut-edge corrosion. This research aims to unravel the self-healing properties observed in these coatings. Through cyclic corrosion tests (CCTs), we compared the corrosion resistance of Zn-Al-Mg coated steel with traditional zinc alloy coatings. Our findings show a notable reduction in corrosion with ZMA4 coatings after 120 CCT cycles. This is due to the formation of corrosion products, namely layered double hydroxides (LDHs) and $Mg(OH)_2$. X-ray diffraction and X-ray photoelectron spectroscopy analyses were employed to confirm the presence of these products and elucidate their roles in the self-healing process. This study highlights the potential of Zn-Al-Mg coatings for enhancing the durability of steel structures in corrosive environments, suggesting a paradigm shift in corrosion protection strategies for marine applications. The development of coatings that exhibit self-healing capabilities in chloride-rich environments could significantly mitigate the challenges posed by cut-edge corrosion, promising extended service life and reduced maintenance costs.

Keywords: Zn-Al-Mg alloy coated steel; corrosion resistance; cyclic corrosion tests; layered double hydroxides; $Mg(OH)_2$

Citation: Kim, S.-H.; Jin, S.-Y.; Yang, J.-H.; Yang, J.-H.; Lee, M.-H.; Yun, Y.-S. Self-Healing Phenomenon at the Cut Edge of Zn-Al-Mg Alloy Coated Steel in Chloride Environments. *Coatings* **2024**, *14*, 485. https://doi.org/10.3390/coatings14040485

Academic Editor: Cecilia Bartuli

Received: 18 March 2024
Revised: 3 April 2024
Accepted: 11 April 2024
Published: 15 April 2024

1. Introduction

Galvanized steel is widely used in various industries due to its excellent corrosion resistance based on sacrificial anode and barrier effects compared with iron and steel [1–3]. Additionally, it is preferred over stainless steel in structures requiring mass installation due to its superior cost effectiveness [3]. Among them, zinc (Zn)-aluminum (Al)-magnesium (Mg) alloy coated steel plates are known to have excellent corrosion resistance, even in marine environments, and are reported to have various advantages [4–8]. Based on these advantages, numerous studies are currently underway. Particularly, in environments with high salt content, stable corrosion products such as zinc chloride hydroxide monohydrate (simonkolleite) are formed on the surface, providing a barrier effect and demonstrating even better corrosion resistance [4,9,10]. However, despite being highly resistant to corrosion and being durable, the possibility of corrosion still exists. Corrosion-induced defects are a major factor affecting the strength reduction of various facilities, and corrosion can lead to the deterioration of facilities, causing safety issues and potential harm to human life [11]. When corrosion occurs, various metals come into contact, accelerating

various types of corrosion, such as galvanic corrosion and contact corrosion, leading to accelerated damage [12]. Therefore, corrosion prevention is crucial. Generally, surfaces possess excellent corrosion resistance, and their corrosion mechanisms have been largely elucidated. In contrast, cut-edge corrosion has a metal-exposed surface in direct contact with the surrounding environment, making it easy for the main factors of corrosion, air and moisture, to come into contact [13,14]. Moreover, galvanic corrosion due to potential differences with surface coatings can occur [15]. Additionally, the increase in corrosion sensitivity can occur through the generation of fine defects or cracks during shearing processes [16,17]. Despite being treated with anti-corrosion measures, cross-section areas have relatively thin coatings formed during the joint formation process, leading to a higher risk of corrosion. Cut-edge corrosion is a more complex issue than surface corrosion. Therefore, in this study, we compared the cut-edge corrosion resistance of steel coated with Zn-Al-Mg alloys, focusing on how varying the proportions of Al and Mg affects this property. Cyclic corrosion tests (CCTs) were conducted to confirm corrosion behavior, and corrosion phenomena were analyzed by the morphology and elemental compositions of the cut edge's corrosion products through field-emission scanning electron microscopy (FE-SEM), energy-dispersive spectrometry (EDS), and an electron probe micro-analysis (EPMA). Additionally, X-ray diffraction (XRD) and X-ray photoelectron spectroscopy (XPS) analyses were conducted to identify the types and bonding states of corrosion products. The purpose of this study was to understand the corrosion reactions occurring in the cut edges of Zn-Al-Mg alloy coated steel and to provide basic design guidelines for producing highly corrosion-resistant materials based on this understanding. It is expected that this will increase the understanding of section corrosion and enable the development of products with even higher durability.

2. Materials and Methods

2.1. Specimens Preparation

The test specimens were supplied by the South Korean company POSCO Steel Corp., Pohang, Republic of Korea. The substrate material selected for this study was low-carbon steel, chosen for its compatibility with the galvanization process. Corrosion tests were carried out on substrates measuring 7.5 cm × 15 cm, which aligns with the standard dimensions required for these tests. For the purpose of materials characterization, sections measuring 1 cm x 1 cm were prepared from the larger substrates. The galvanization process involved immersing the steel substrates in a molten Zn-Al-Mg bath. The bath temperature was meticulously controlled at 430–500 °C, and the immersion time was set to ensure a uniform and consistent coating across all samples. This approach was adopted to simulate real-world industrial conditions as closely as possible, providing a solid foundation for the assessment of the Zn-Al-Mg coating's corrosion resistance properties [18,19]. As shown in Table 1, the test specimens consisted of Zn-plated steel sheets (Zn about 98~100 wt.%) and two types of Zn-Al-Mg specimens with different elemental compositions, designated as ZA, ZMA2, and ZMA4, respectively. The test specimens had almost identical coating weights (approximately 275~300 g/m^2) and were obtained by shearing processing to obtain cut edges. Prior to various analyses, the test specimens were degreased using sodium hydroxide (NaOH) to remove impurities, followed by cleaning in acetone and ethanol (C_2H_5OH) for 10 min each. Subsequently, the test specimens were rinsed with distilled water with a resistance value of 18.2 MΩ·cm and allowed to air dry.

Table 1. The elemental composition of the test specimens.

Specimens	Zn (wt.%)	Al (wt.%)	Mg (wt.%)
ZA	98~100	0~2	-
ZMA2	93~97	1~3	2~4
ZMA4	81~86	10~13	4~6

2.2. Corrosion Tests

The corrosion resistance of ZA, ZMA2, and ZMA4 specimens was evaluated using a CCT (Q-FOG CCT-1100, Q-LAB, U.S.A) in accordance with the ASTM B 117 standard [20]. Each cycle involved spraying a 5% sodium chloride (NaCl) solution at 35 °C for 2 h, followed by drying at 60 °C for 4 h and then maintaining a humidity of 95% RH for an additional 2 h. For this study, three specimens of each type were used, all of which displayed similar trends in corrosion behavior. Among these, a representative specimen was chosen for detailed illustration in Figure 1. Specimens were briefly extracted from the CCT chamber at intervals of approximately every 10 cycles for photographic documentation and were then immediately repositioned in the chamber for continued testing. This procedure was conducted until red rust appeared on the specimens, which was observed at up to 160 cycles.

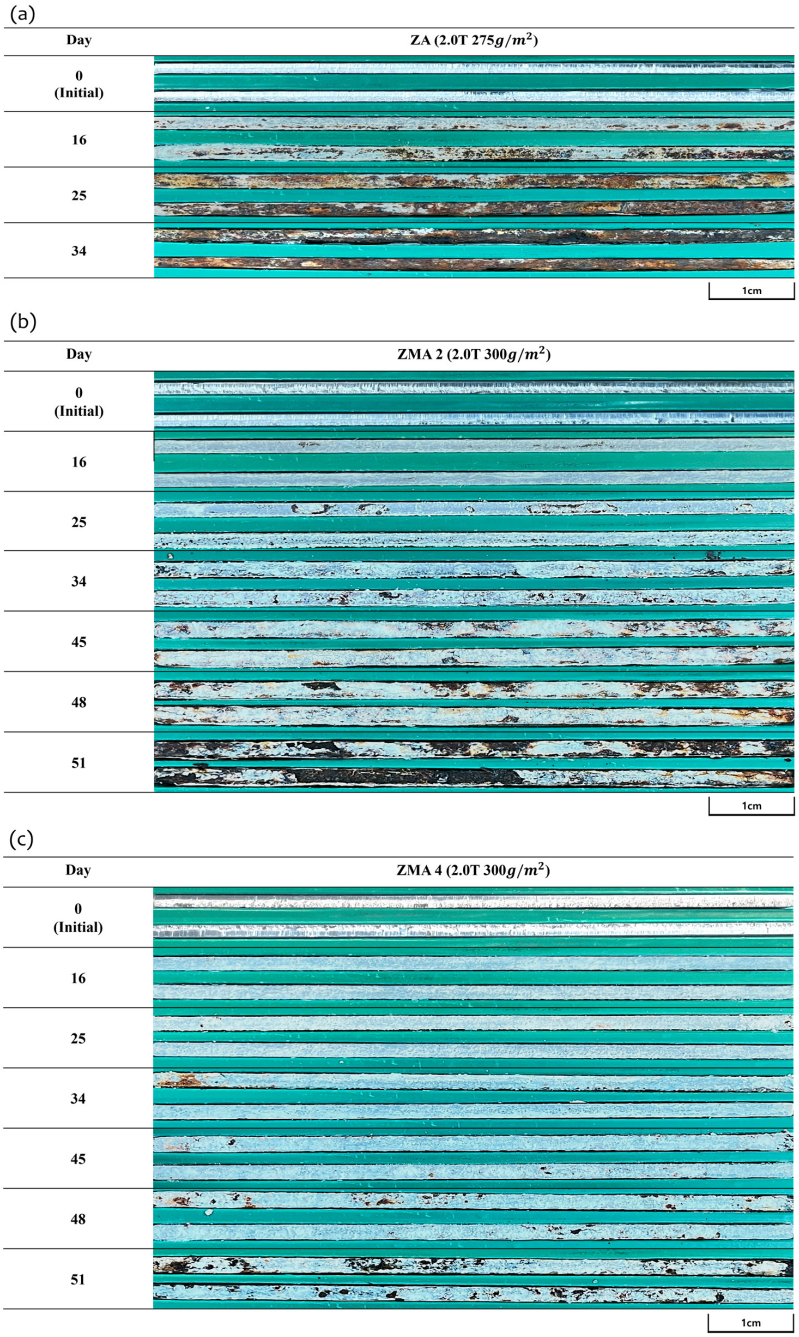

Figure 1. Images capturing the onset of rust formation, taken using a digital camera. (**a**) ZA, (**b**) ZMA2, (**c**) ZMA4.

2.3. Materials Characterization

To examine the cut edge morphology of the test specimens, an optical microscope (OM, AM4113ZT, Dino-Lite, Los Angeles, CA, USA) and FE-SEM (CLARA, Tescan Brno, Brno-Kohoutovice, Czech Republic) with an accelerating voltage of 20 kV were used. Elemental composition and distribution were analyzed using EDS attached to the FE-SEM equipment, and EPMA (JXA-8230, JEOL, Tokyo, Japan) was employed. The EPMA utilized an accelerating voltage of 15 kV, with an electron beam intensity set to 1.999E-0.08A and a beam size of 4 μm for analysis. XRD (SmartLab, Rigaku, Tokyo, Japan) utilizing Cu Kα radiation (λ = 1.5418 Å, 40 kV, 200 mA) and a scanning speed of 1° min−1 over a 2θ range of 10–90° was employed to characterize the crystalline composition of the coatings. Surface chemistry was analyzed using XPS (AXIS SUPRA, KRATOS Analytical Ltd., Manchester, UK) with Al Kα radiation (1486.6 eV, 20 kV, 15 mA). Binding energies were calibrated using the C1s peak at 284.8 eV.

3. Results and Discussion

Initially, accelerated corrosion tests were conducted using CCT to visually observe the corrosion behavior of ZA, ZMA2, and ZMA4. Figure 1 shows the results captured with a digital camera until the occurrence of initial rust formation on ZA, ZMA2, and ZMA4.

As shown in Figure 1, the ZA specimen exhibited severe corrosion phenomena on the 34th day, while the ZMA2 specimen, with higher Mg and Al content, demonstrated better intergranular corrosion resistance. Additionally, it was observed that even after 51 days, the area affected by rust in the ZMA4 specimen was relatively small compared with the other specimens, indicating that higher Mg and Al contents contribute to better corrosion resistance. Furthermore, in the case of ZMA4, the pattern of rust formation observed on the 34th day was weakened at 45 and 48 days before intensifying again on the 51st day. Similar observations were made for ZMA2, where the formation of red rust was observed; however, on the 34th day, a white film was formed, somewhat obscuring this phenomenon. These observations suggest that the addition of Mg and Al in ZMA2 and ZMA4 led to the occurrence of self-healing phenomena through the formation of white corrosion products [21]. Based on the images of rust formation obtained through CCT in Figure 1, the area ratio of the corrosion area was measured using the DBSCAN method and is presented in Figure 2 [22].

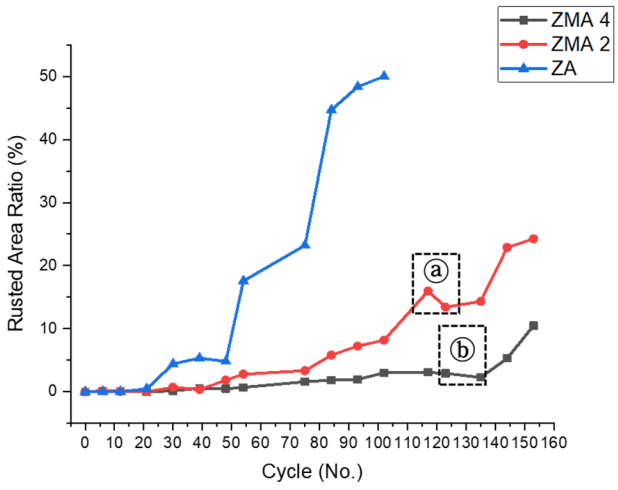

Figure 2. Measurement graph of rusted area in cyclic corrosion test: ZMA4, ZMA2, and ZA.

Similarly to the visible reduction in the area of rust observed in ZMA2 and ZMA4 specimens, image analysis revealed a decrease in the proportion of rust area in sections a and b. When comparing the 34th day (102 Cycles) with the ZA specimen, ZMA4 showed a proportion of approximately 3.01%, ZMA2 showed 8.18%, and ZA showed a rust proportion of 50.02%, indicating that Zn-Al-Mg alloy coating exhibits superior corrosion resistance in

highly corrosive environments. Figure 3, which shows the morphology of the cut edge after 100 cycles of the CCT observed through OM, suggests that the white corrosion products on the surface of ZMA2 and ZMA4 may have a masking effect. This trend prompted further analysis before and after 100 cycles of the CCT.

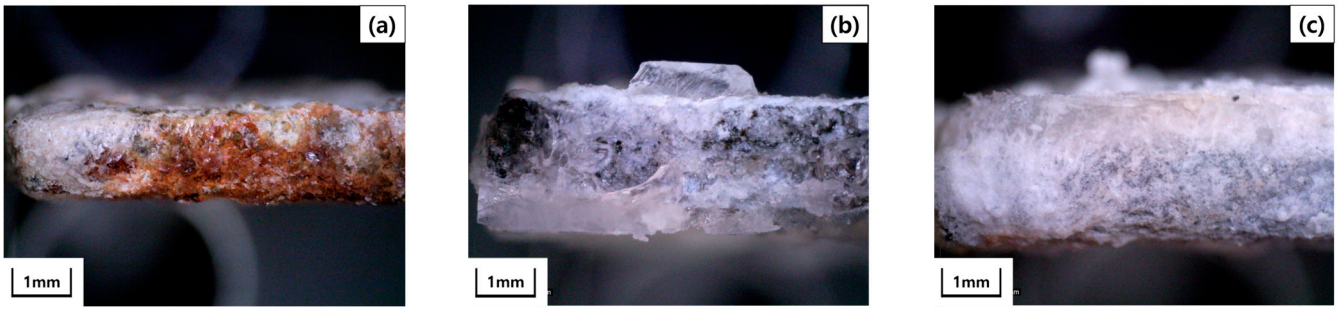

Figure 3. Appearance of corrosion morphologies under the optical microscope: (**a**) ZA, (**b**) ZMA2, and (**c**) ZMA4.

Figure 4 presents the morphology images of the cut edges observed using the backscattered electron (BSE) mode of FE-SEM. Examination of the initial morphology of the cut edges before corrosion, up to (a–c) in Figure 4, revealed minimal damage to the cut edge of the ZA specimen, with no discernible shapes indicative of other compounds. However, relatively diverse shapes of intermetallic compounds were observed in ZMA2 and ZMA4 specimens. This is attributed to the presence of common phases in Zn-Al-Mg alloy coated steel produced via the hot-dipping method, including the Zn-matrix phase, binary phases such as Zn-$MgZn_2$, Zn-Mg_2Zn_{11}, and Zn-Al, and ternary phases such as Zn-$MgZn_2$-Al [2].

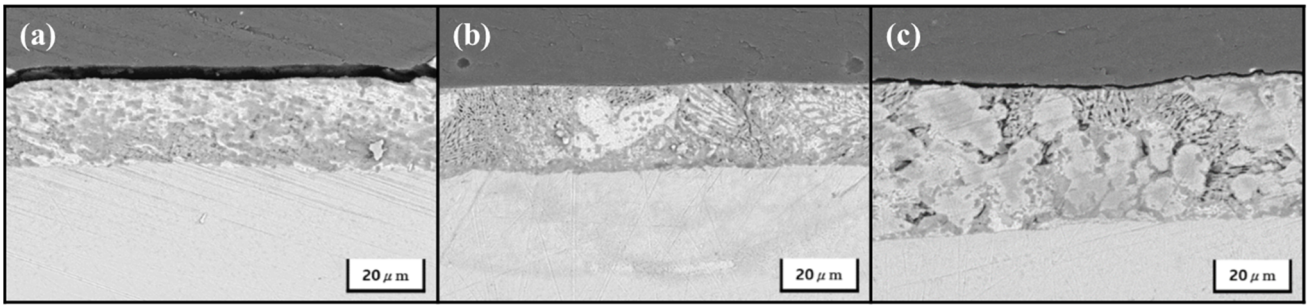

Figure 4. SEM image of the specimens (**a**) ZA, (**b**) ZMA2, and (**c**) ZMA4 for initial state.

For the analysis of the morphology after 100 cycles of the CCT, Figure 5 illustrates SEM images of the cut edges. Compared with the initial state, significant cracks were observed in the ZA and ZMA2 specimens, indicating notable changes in the morphology of the cut edges. ZMA4 exhibited a similar morphology even after 100 cycles, with the lamellar structure of intermetallic compounds observed in the initial morphology remaining visible after 6 months, along with a peculiar leaf-like feature. These microstructures of intermetallic compounds were determined to be binary phases of Al-$MgZn_2$ with a hexagonal close-packed structure [23]. A point EDS analysis was conducted on each specimen to examine the elemental composition of the detailed cut-edge morphology after 100 cycles of the CCT.

Figure 6 and Tables 2–4 present the morphology and elemental composition of the specimens after 100 cycles of combined corrosion testing. As shown in Figure 6a and Table 2, Zn was hardly detected in any measured areas of ZA, while a high distribution of iron (Fe) was observed in all analysis points. This indicates that as corrosion progresses, the alloy coating is consumed, revealing the internal structure of the steel, prominently manifesting the presence of Fe.

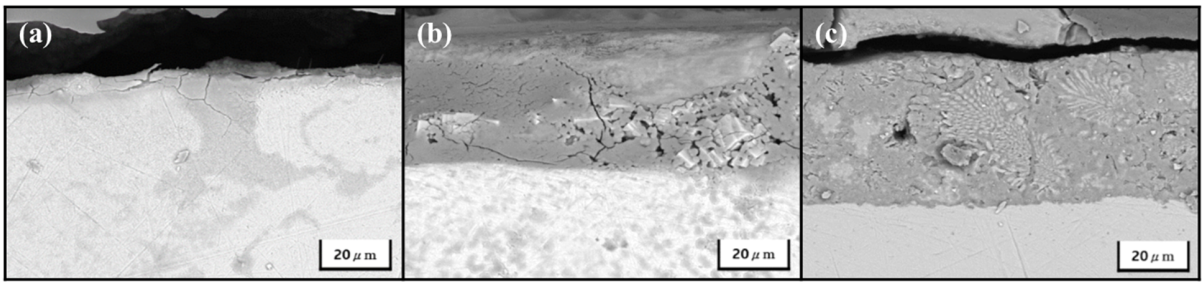

Figure 5. SEM image of the specimens (**a**) ZA, (**b**) ZMA2, and (**c**) ZMA4 after 100 cycles of the CCT.

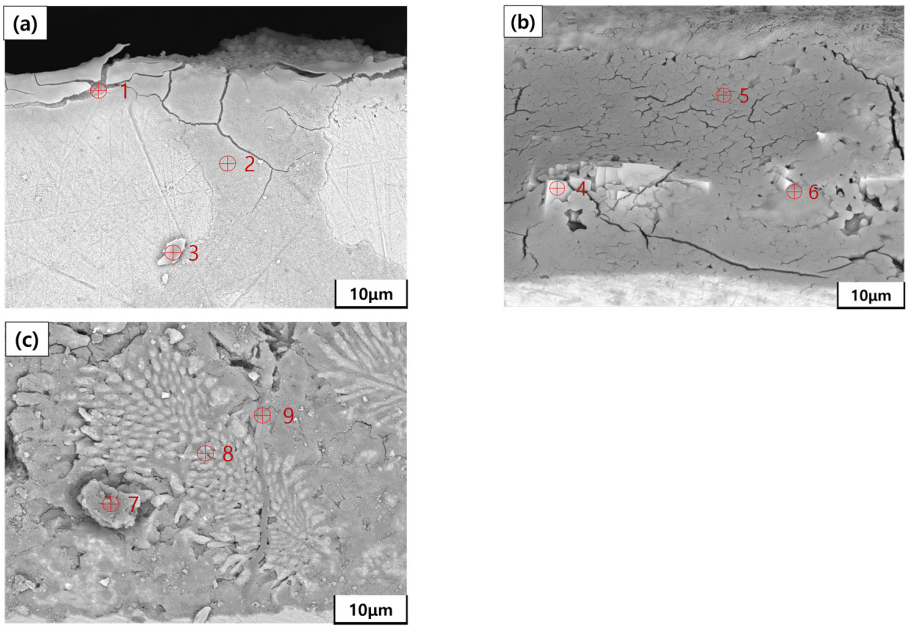

Figure 6. Point EDS results of specimens, (**a**) ZA, (**b**) ZMA2, and (**c**) ZMA4.

Table 2. EDS quantitative analysis at each point marked in Figure 6a.

Point	Zn (wt.%)	Al (wt.%)	Mg (wt.%)	Fe (wt.%)	O (wt.%)
1	3.82	-	-	78.46	17.72
2	-	-	-	96.26	3.74
3	-	-	-	91.38	8.62

Table 3. EDS quantitative analysis at each point marked in Figure 6b.

Point	Zn (wt.%)	Al (wt.%)	Mg (wt.%)	Fe (wt.%)	O (wt.%)
4	44.90	-	-	7.95	47.15
5	-	-	-	23.93	76.07
6	14.72	12.67	-	22.31	50.30

Table 4. EDS quantitative analysis at each point marked in Figure 6c.

Point	Zn (wt.%)	Al (wt.%)	Mg (wt.%)	Fe (wt.%)	O (wt.%)
7	35.19	9.70	-	4.16	50.95
8	41.90	46.95	-	2.66	8.49
9	57.86	0.25	0.17	2.53	39.19

Figure 6b and Table 3 show the SEM and EDS results of ZMA2 after 100 cycles of combined corrosion testing. Compared with ZA, a relatively larger amount of Zn and Al was observed, indicating slightly better corrosion resistance. Zn was detected at point 4, while no metallic components of the alloy coating were found at points 2 and 3 in ZA. However, Zn and Al were detected at point 6. The elemental composition at point 6 suggests corrosion occurring on an Al phase with Zn in solid solution.

Similarly, when analyzed after 100 cycles, ZMA4 (Figure 6c and Table 4) exhibited the highest content of metallic elements in the alloy coating compared with ZA and ZMA2, indicating the best corrosion resistance among the three specimens. Fe content was notably low at all analysis points, with points 7 and 8 showing an Al phase with Zn in varying proportions and point 9 indicating Zn containing Mg and Al. This is consistent with reports suggesting that Zn and Al interact to enhance the corrosion resistance of the alloy. Additionally, while Mg was undetectable in ZMA2, only trace amounts were observed in ZMA4, suggesting that Mg ions are the first to leach out, forming stable corrosion products and delaying the leaching of Zn and Al, thereby enhancing corrosion resistance [9,21].

To examine the distribution of elemental composition on the specimen surface as corrosion progresses, an EPMA mapping analysis was conducted. Livetime, the average duration of activation of the X-ray detector, was utilized to graphically represent the ratio of elements appearing in the corrosion products along the depth direction from the coating surface to the substrate. EPMA mapping analyzes the X-rays emitted from each pixel, providing insights into the distribution of elements such as Zn, Al, Mg, Fe, chloride (Cl), and oxygen (O) [24]. The left side of the livetime measurement represents the coating layer, while the right side represents the substrate. This allowed for the evaluation of the corrosion products of each specimen and an assessment of the influence of alloy elements on the corrosion behavior.

Upon examination of Figure 7, the elemental composition present within each specimen's coating layer was identified. In Figure 7b,c, the presence of Mg layers in ZMA2 and ZMA4 is evident, with ZMA4 exhibiting the darkest shade for Al. Regarding Zn layers, Figure 7a mapping indicates that ZA had the highest proportion. To conduct a more quantitative assessment, the initial EPMA analysis values were graphed using livetime values, as shown in Figure 8.

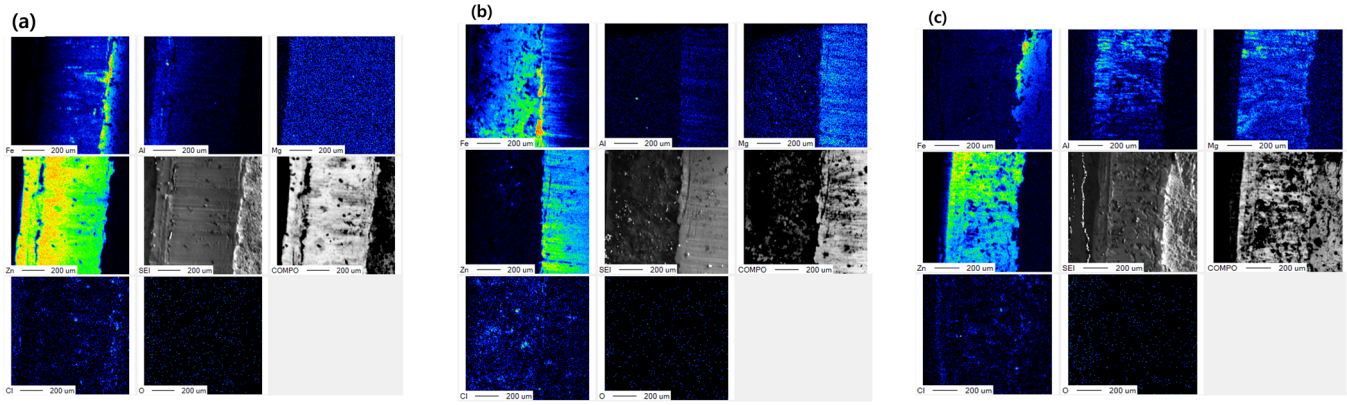

Figure 7. EPMA mapping image of the specimens (**a**) ZA, (**b**) ZMA2, and (**c**) ZMA4 for initial state.

As observed in Figure 8a, ZA exhibited a significant presence of Zn, as indicated by the strong red and yellow signals in the EPMA mapping of Zn. A high peak of Fe was identified at approximately 230 points, indicating the end of the coating layer. Upon examining the graph of ZMA2 in Figure 8b, it was evident that Zn was distributed prominently, with Mg and Al also being present near the surface. The thinner coating layer in ZMA2 reflected in the graph may be attributed to a slight bias in EPMA measurements during analysis, as well as variations that can occur during the shearing process, leading to random variations in coating thickness across specimens. Similarly, ZMA4 also exhibited a generally high

elemental composition of Zn, Mg, and Al, with Zn signals being notably lower than in ZA, while Al and Mg showed the strongest signals, indicating their presence distinctly. Comparing the maximum values of each component in the respective graphs, ZA showed values of 90.22 for Zn, 4.25 for Al, and 27.63 for Fe. In contrast, ZMA2 exhibited values of 23.30 for Zn, 0.87 for Al, 1.98 for Mg, and 47.75 for Fe, while ZMA4 showed values of 30.82 for Zn, 4.28 for Al, 2.66 for Mg, and 11.32 for Fe. Despite the arbitrary proportion of iron in each specimen, ZMA2 and ZMA4 demonstrated ratios of Al-Mg similar to the actual elemental composition, indicating the formation of Al-Mg ratios in these alloys.

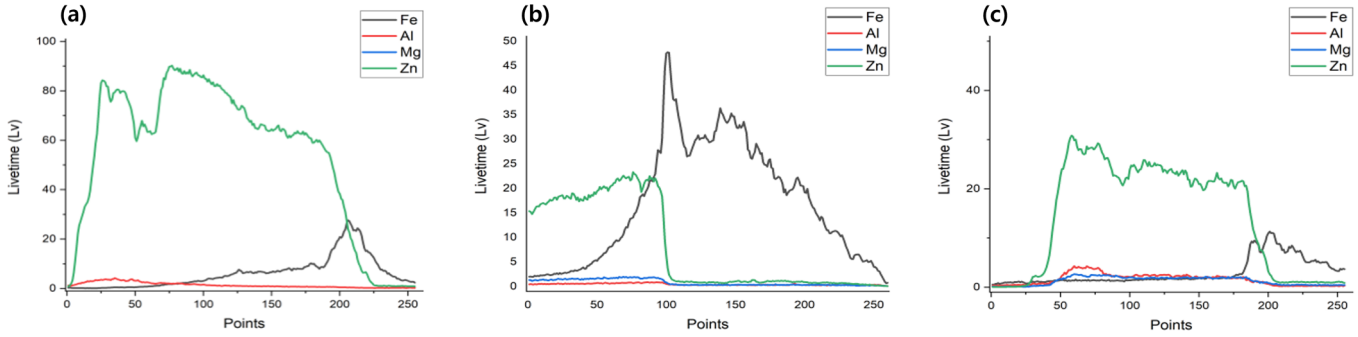

Figure 8. The average livetime values graph of the EPMA raw data in the initial state. (**a**) ZA, (**b**) ZMA2, (**c**) ZMA4.

Figure 9 revealed the elemental distribution on the cut edges following 100 cycles of corrosion. The EPMA mapping of ZA specimens indicated a descent of maximum Zn values from the coating layer surface into some depth, with the strongest signals shifting between the surface and the interface. Al layers were not prominently observed, while Cl and Fe exhibited irregular distributions, indicating the corrosion phenomenon in ZA specimens. In Figure 9b, the EPMA results of ZMA2 specimens showed strong Zn signals beneath the coating layer. Al distribution was observed only near the surface, while Mg appeared to distribute over a wider area compared with Al. Upon observing the EPMA mapping of ZMA4 in Figure 9c, it was noted that the distribution patterns of Fe and Mg were nearly identical. Al was observed only in the surface layer, and Zn exhibited weaker signals in areas where Fe and Mg showed stronger signals. To further analyze the results, Figure 10 graphs the EPMA mapping of Figure 9. In Figure 10a, the graph for ZA demonstrates a significant overall increase in Fe values compared with the initial stage, with Zn showing maximum values near the coating layer and the interface. For ZMA2, generally high Zn values were observed, with Al values being high only near the surface. Similarly, in ZMA4, Mg and Fe exhibited high intensities in similar regions, while Al showed high values near the surface. This suggests the importance of Mg in cut-edge corrosion. Comparing the overall graphs, the maximum Zn values appeared in the order of ZMA4, ZMA2, and ZA. Notably, in ZMA2 and ZMA4, as the corrosion progressed, Al components appeared to move toward the surface. Particularly high Mg values in ZMA4 emphasize the importance of Mg in cut-edge corrosion. Considering corrosion resistance and lifespan, the specimen ranking was observed as ZMA4 > ZMA2 > ZA, indicating ZMA4's superior corrosion resistance and lifespan compared with ZA, which appeared relatively more susceptible to corrosion. Such analyses play a crucial role in understanding the various factors influencing corrosion and corrosion resistance.

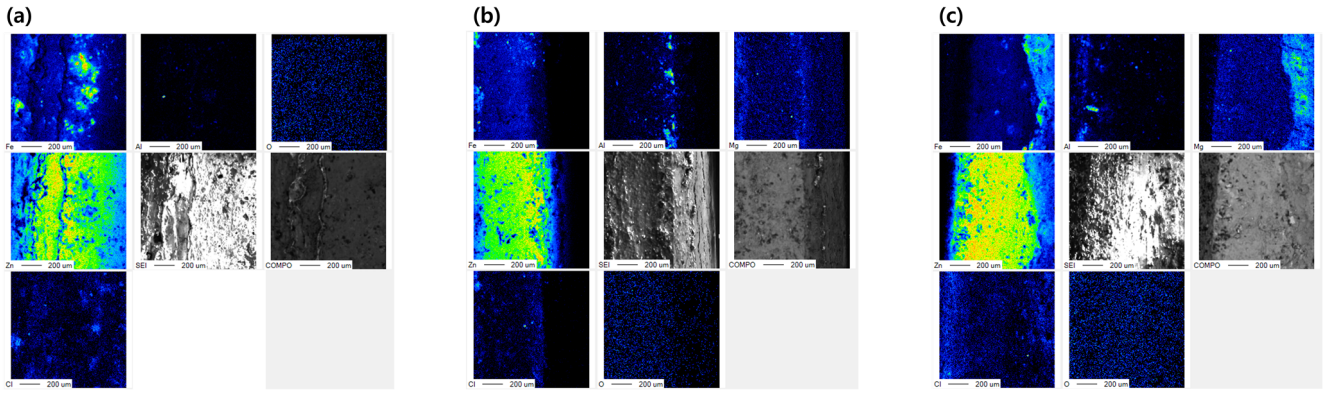

Figure 9. EPMA mapping image of the specimens (**a**) ZA, (**b**) ZMA2, and (**c**) ZMA4 after 100 cycles.

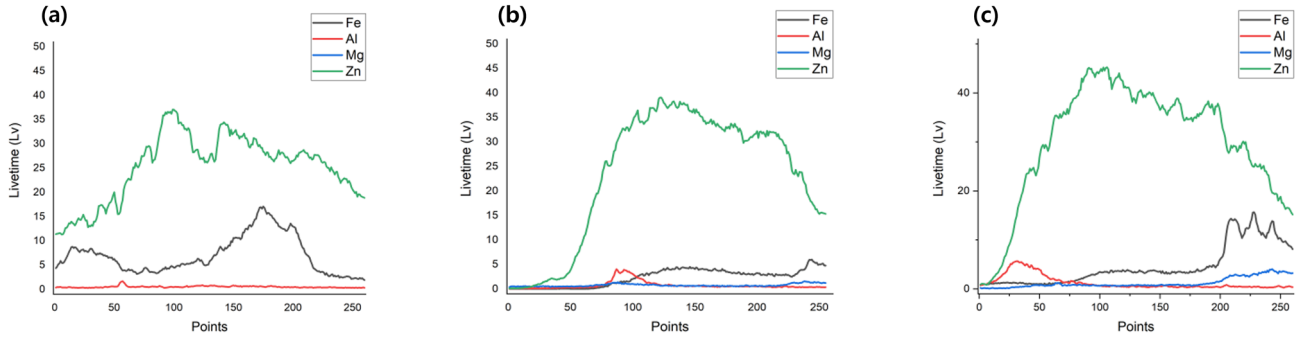

Figure 10. The average livetime values graph of the EPMA raw data after 100 CCT cycles. (**a**) ZA, (**b**) ZMA2, (**c**) ZMA4.

Based on the previous results, the test specimen exhibiting the best corrosion resistance on the cut surface was inferred to be ZMA4. When investigating ZMA4 to identify the factors contributing to its excellent corrosion resistance on the cut surface, an increase in corrosion products containing Mg was found to contribute to the enhancement of corrosion resistance. To clearly understand the crystal structure and chemical state of these corrosion products, XRD and XPS analyses were conducted. Samples for analysis were prepared by grinding the cut edges of the corroded test specimens into powder form. Figure 11 illustrates the XRD results of the test specimens, and Table 5 indicates the bonding states corresponding to each peak number. Upon examining ZA, the main peaks observed were reported to be simonkolleite and zincite (ZnO), commonly detected corrosion products in Zn-coated steel known to enhance corrosion resistance. Simonkolleite, known for its relatively high environmental stability, is presumed to have played a significant role in corrosion prevention in ZA coatings. In the case of ZMA2, a peak corresponding to the (Mg, Zn)-Al layered double hydroxide (LDH) structure was found at 23.23°. The LDH structure likely provided a more stable environment than ZA, contributing to its high corrosion resistance [25,26]. Additionally, peaks corresponding to simonkolleite and aluminum oxide (Al_2O_3) were observed. The presence of Mg is believed to have sustained the stability of simonkolleite in ZMA2 [27]. These factors suggest that ZMA2 exhibited additional corrosion resistance compared with ZA coatings. ZMA4 was found to include a broader range of corrosion products. Peaks corresponding to the (Mg, Zn)-Al LDH structure were detected around the 23.23° and 24.96° angles, and peaks corresponding to $Mg(OH)_2$ were observed at 18.53° and 43.06°. This suggests that ZMA4 coatings formed self-healing products during corrosion testing [21]. Furthermore, zinc chlorate hydrate ($Zn(ClO_2)_2(H_2O)_2$) peaks were observed at 31.82° and 55.34°, indicating the presence of intermediate products before further corrosion to ZnO. This evidence suggests that additional time is required for the corrosion process of ZMA4 coatings to complete. Therefore, ZMA4 coatings not

only provide strong corrosion resistance due to their physical properties but also possess effective mechanisms for healing corrosion when it occurs.

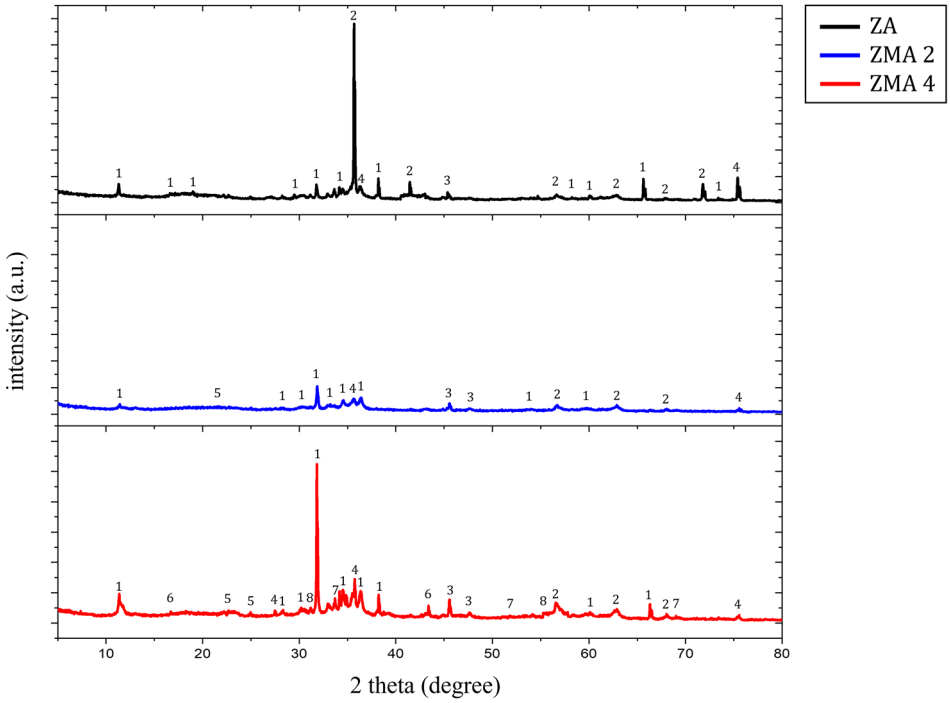

Figure 11. XRD results of ZA, ZMA2, and ZMA4.

Table 5. Chemical bonding by peak number in the XRD results.

Label	Name	Chemical Formula	Label	Name	Chemical Formula
1	Simonkolleite	$Zn_5(OH)_8Cl_2H_2O$	5	LDH	$[M(II)_{1-x}{\cdot}M(III)_x(OH)_2]^{x+}[A^{n-}]_{x/n}$, $M(II) = Zn^{2+}, Mg^{2+}$, $M(III) = Al^{3+}$
2	Zincite, Zinc Oxide	ZnO	6	Magnesium Hydroxide	$Mg(OH)_2$
3	Zinc Hydroxide	$Zn(OH)_2$	7	Magnesium Hydroxide Chloride	$Mg_2(OH)_3Cl$
4	Aluminum Oxide	Al_2O_3	8	Zinc Chlorate Hydrate	$Zn(ClO_2)_2(H_2O)_2$

Figure 12 shows the XPS spectra of Mg 2p in ZMA2 and ZMA4 samples, where the alloy steel contains 2% and 4% of Mg, respectively, and the analysis was conducted after converting the corrosion products into powder form. To investigate the cause of the observed increase in Mg distribution on the plate due to corrosion progression as seen in the EPMA analysis images, this study performed measurements for Mg 2p using this method. The XPS analysis results reveal a strong peak at 49.50 eV, indicating the presence of $Mg(OH)_2$ and MgO. Both compounds demonstrate Mg in a 2+ oxidation state through bonding with O, underscoring Mg's crucial role in the corrosion process. Considering the EPMA, XRD, and XPS results collectively, they suggest that the presence of $Mg(OH)_2$ bonding plays a significant role in this process. This increase underscores Mg's protective role in the corrosion resistance of Zn-based alloy-coated steel, emphasizing the crucial role of Mg in this context.

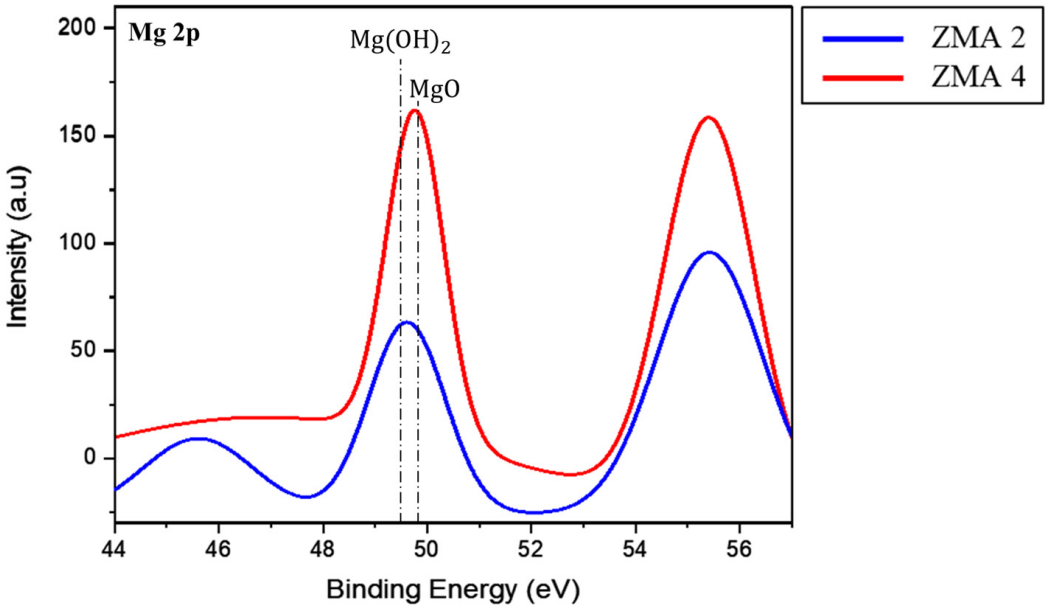

Figure 12. XPS results of ZA, ZMA2, and ZMA4.

Upon comprehensive analysis of the study's results, it was observed that ZMA4 exhibited the best corrosion resistance, primarily attributed to the presence of LDH and $Mg(OH)_2$. Such self-healing reactions were presumed to occur as depicted in Figure 13, where in the case of Zn-Al-Mg alloy coating, Zn and Mg corrode in the environment to form ions such as Zn^{2+} and Mg^{2+}, which react with ionized oxygen to generate hydroxide ions. during the corrosion process, the $MgZn_2$ phase was found to be the most reactive, contributing to the anodic reaction, while the Al-rich phase was expected to contribute to the cathodic reaction [28,29]. The occurrence of corrosion defects was mainly attributed to anodic dissolution, inducing the generation of hydroxide ions as electrons are transferred to the cathodic region. The resulting pH difference can significantly influence the corrosion process, where an increase in pH can lead to the formation of corrosion products [30]. In an alkaline environment with high pH, $Mg(OH)_2$ is reported to remain stable as it does not undergo further chemical reactions [31], but in chloride environments, $Mg(OH)_2$ can continue to corrode, forming $MgCl_2$ along with $Mg_2(OH)_3Cl$. In this process, Mg remains in the form of oxide at high pH, attributed to the common-ion effect where the solubility of Mg oxide decreases due to the presence of hydroxide ions [32]. Subsequently, the dissolution of aluminum to form $Al(OH)^{4-}$ was expected to induce the instability of hydrated oxides [31]. Although LDH was detected in ZMA2 and ZMA4 after 100 CCT cycles, ZnO was not as prominently observed compared with ZA. ZnO typically forms as a result of Zn corrosion and is recognized as a late-stage product of corrosion, but in this case, LDH or $Zn(OH_{)2}$ and other compounds were formed instead of ZnO, which is presumed to be related to the presence of Mg^{2+} [33,34]. EPMA results confirmed the leaching of Mg from the surface, which is presumed to enhance the formation of individual $Mg(OH)_2$ through the use of Mg as a pH buffer. Similar trends were observed compared with studies demonstrating higher self-healing properties in environments containing chloride ions [35].

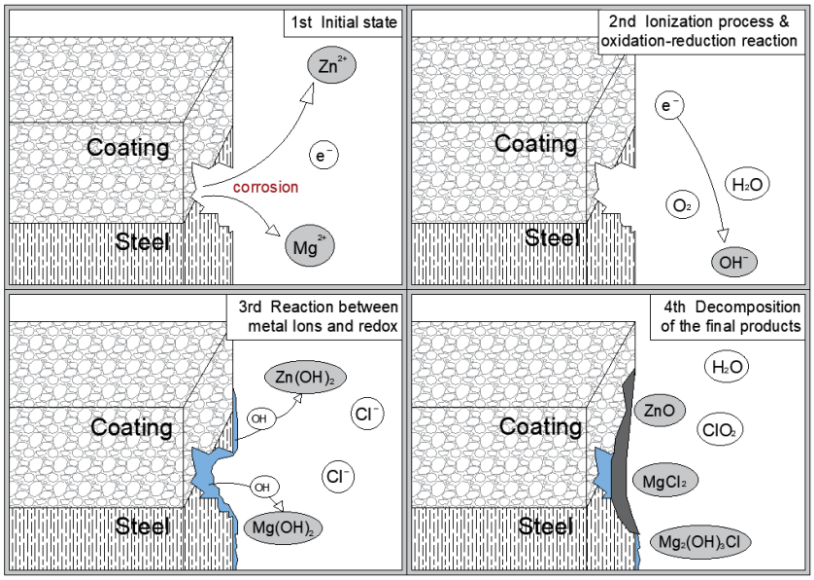

Figure 13. Cut-edge corrosion behavior of Zn-Al-Mg alloy coated steel.

4. Conclusions

In this study, the corrosion reactions and corrosion resistance of Zn-Al-Mg alloy-coated steel plate cut edges were analyzed. When subjected to CCT corrosion tests, ZMA4 exhibited superior corrosion resistance compared with ZA and ZMA2. The results of the CCT experiments showed a decrease in the corrosion area for ZMA2 and ZMA4 at around 120 cycles. Additionally, after 100 CCT cycles, the distribution of Mg components on the cut edge of ZMA4 specimens was observed, and an XRD analysis confirmed peaks of corrosion products contributing to the self-healing mechanism, such as LDH and $Mg(OH)_2$ in ZMA4. Self-healing reactions can enhance the corrosion resistance of cut edges through methods such as LDH coating or precipitation and reactions of Mg ions within the coating layer. However, continuous exposure of ZMA alloy-coated cut edges in chloride environments may damage the formed $Mg(OH)_2$, leading to corrosion of the alloy containing Mg in chloride environments. Therefore, the development of coatings with superior corrosion resistance on cut edges is warranted.

Author Contributions: Conceptualization, J.-H.Y. (Ji-Hoon Yang); Validation, J.-H.Y. (Ji-Hoon Yang), J.-H.Y. (Jeong-Hyeon Yang) and Y.-S.Y.; Formal analysis, S.-H.K. and S.-Y.J.; Data curation, J.-H.Y. (Ji-Hoon Yang); Writing—original draft, S.-H.K.; Writing—review & editing, S.-H.K. and S.-Y.J.; Supervision, J.-H.Y. (Jeong-Hyeon Yang), M.-H.L. and Y.-S.Y.; Project administration, Y.-S.Y. All authors have read and agreed to the published version of the manuscript.

Funding: This research received no external funding.

Institutional Review Board Statement: Not applicable.

Informed Consent Statement: Not applicable.

Data Availability Statement: The data presented in this study are not available due to privacy.

Conflicts of Interest: Seo-Yun Jin and Ji-Hoon Yang were employed by Sewon America and POSCO, respectively. The remaining authors declare that the research was conducted in the absence of any commercial or financial relationships that could be construed as a potential conflict of interest.

References

1. Shibli, S.; Meena, B.N.; Remya, R. A review on recent approaches in the field of hot dip zinc galvanizing process. *Surf. Coat. Technol.* **2015**, *262*, 210–215. [CrossRef]
2. Dutta, M.; Halder, A.K.; Singh, S.B. Morphology and properties of hot dip Zn–Mg and Zn–Mg–Al alloy coatings on steel sheet. *Surf. Coat. Technol.* **2010**, *205*, 2578–2584. [CrossRef]

3. Yeomans, S.R. Galvanized Steel Reinforcement: Recent Developments and New Opportunities. In Proceedings of the 5th International Federation for Structural Concrete, Melbourne, VIC, Australia, 7–11 October 2018; pp. 7–11.
4. Diler, E.; Rouvellou, B.; Rioual, S.; Lescop, B.; Vien, G.N.; Thierry, D. Characterization of corrosion products of Zn and Zn–Mg–Al coated steel in a marine atmosphere. *Corros. Sci.* **2014**, *87*, 111–117. [CrossRef]
5. Stoulil, J.; Prosek, T.; Nazarov, A.; Oswald, J.; Kriz, P.; Thierry, D. Electrochemical properties of corrosion products formed on Zn-Mg, Zn-Al and Zn-Al-Mg coatings in model atmospheric conditions. *Mater. Corros.* **2015**, *66*, 777–782. [CrossRef]
6. Rai, P.K.; Rout, D.; Kumar, D.S.; Sharma, S.; Balachandran, G. Corrosion behaviour of hot-dip Zn-Al-Mg coatings with different Al content. *Anti-Corros. Methods Mater.* **2022**, *69*, 29–37. [CrossRef]
7. Ye, C.; Jia, L.; Xu, G.; Wang, F.; Wang, X.; Zhang, H. Microstructure and initial corrosion behavior of double-layer Zn-Al-Mg coatings produced by PVD. *Surf. Coat. Technol.* **2019**, *366*, 214–226. [CrossRef]
8. Bakhsheshi-Rad, H.R.; Hamzah, E.; Low, H.T.; Kasiri-Asgarani, M.; Farahany, S.; Akbari, E.; Cho, M.H. Fabrication of biodegradable Zn-Al-Mg alloy: Mechanical properties, corrosion behavior, cytotoxicity and antibacterial activities. *Mater. Sci. Eng. C* **2017**, *73*, 215–219. [CrossRef] [PubMed]
9. Yao, C.; Lv, H.; Zhu, T.; Zheng, W.; Yuan, X.; Gao, W. Effect of Mg content on microstructure and corrosion behavior of hot dipped Zn–Al–Mg coatings. *J. Alloys Compd.* **2016**, *670*, 239–248. [CrossRef]
10. Duchoslav, J.; Steinberger, R.; Arndt, M.; Keppert, T.; Luckeneder, G.; Stellnberger, K.H.; Hagler, J.; Angeli, G.; Riener, C.K.; Stifter, D. Evolution of the surface chemistry of hot dip galvanized Zn–Mg–Al and Zn coatings on steel during short term exposure to sodium chloride containing environments. *Corros. Sci.* **2015**, *91*, 311–320. [CrossRef]
11. Sanni, O.; Iwarere, S.A.; Daramola, M.O. Introduction: Corrosion basics and corrosion testing. In *Electrochemical and Analytical Techniques for Sustainable Corrosion Monitoring*; Elsevier: Amsterdam, The Netherlands, 2023; pp. 1–23.
12. Chen, H.; Lv, Z.; Lu, L.; Huang, Y.; Li, X. Correlation of micro-galvanic corrosion behavior with corrosion rate in the initial corrosion process of dual phase steel. *J. Mater. Res. Technol.* **2021**, *15*, 3310–3320. [CrossRef]
13. Sheikholeslami, S.; Williams, G.; McMurray, H.N.; Gommans, L.; Morrison, S.; Ngo, S.; Williams, D.E.; Gao, W. Cut-edge corrosion behavior assessment of newly developed environmental-friendly coating systems using the Scanning Vibrating Electrode Technique (SVET). *Corros. Sci.* **2021**, *192*, 109813. [CrossRef]
14. Yıldız, R.; Dehri, I. Investigation of the cut-edge corrosion of organically-coated galvanized steel after accelerated atmospheric corrosion test. *Arab. J. Chem.* **2015**, *8*, 821–827. [CrossRef]
15. Marques, A.G.; Izquierdo, J.; Souto, R.M.; Simões, A.M. SECM imaging of the cut edge corrosion of galvanized steel as a function of pH. *Electrochim. Acta* **2015**, *153*, 238–245. [CrossRef]
16. Turnbull, A.; Mingard, K.; Lord, J.D.; Roebuck, B.; Tice, D.R.; Mottershead, K.J.; Fairweather, N.D.; Bradbury, A.K. Sensitivity of stress corrosion cracking of stainless steel to surface machining and grinding procedure. *Corros. Sci.* **2011**, *53*, 3398–3415. [CrossRef]
17. Worsley, D.A.; Williams, D.; Ling, J. Mechanistic changes in cut-edge corrosion induced by variation of organic coating porosity. *Corros. Sci.* **2001**, *43*, 2335–2348. [CrossRef]
18. Son, I.R.; Kim, T.C.; Ju, G.I.; Kim, M.S.; Kim, J.S. Development of PosMAC® Steel and Its Application Properties. *Korean J. Met. Mater.* **2021**, *59*, 613–623. [CrossRef]
19. Kim, T.C.; Kim, S.H.; Kim, S.Y.; Oh, M.S.; Yu, B.H.; Kim, J.S. Hot dip Zn-Al-Mg Alloy Plated Steel Sheet Having Excellent Corrosion Resistance and Method for Manufacturing. K.R. Patent 101,568,509, 20 November 2015.
20. *ASTM B117-03*; Standard Practice for Operating Salt Spray Apparatus. ASTM: West Conshohocken, PA, USA, 2003.
21. Krieg, R.; Rohwerder, M.; Evers, S.; Schuhmacher, B.; Schauer-Pass, J. Cathodic self-healing at cut-edges: The effect of Zn_2 and Mg_2 ions. *Corros. Sci.* **2012**, *65*, 119–127. [CrossRef]
22. Kim, B.S.; Kim, Y.W.; Lee, K.H.; Yang, J.H. Corrosion image analysis on galvanized steel by using superpixel DBSCAN clustering algorithm. *Korean Inst. Surf. Eng.* **2022**, *55*, 164–172.
23. Yao, C.; Tay, S.L.; Zhu, T.; Shang, H.; Gao, W. Effects of Mg content on microstructure and electrochemical properties of Zn–Al–Mg alloys. *J. Alloys Compd.* **2015**, *645*, 131–136. [CrossRef]
24. Hodoroaba, V.; Kim, K.J.; Unger, W.E. Energy dispersive electron probe microanalysis (ED-EPMA) of elemental composition and thickness of Fe-Ni alloy films. *Surf. Interface Anal.* **2012**, *44*, 1459–1461. [CrossRef]
25. Ishikawa, T.; Matsumoto, K.; Kandori, K.; Nakayama, T. Synthesis of layered zinc hydroxide chlorides in the presence of Al (III). *J. Solid State Chem.* **2006**, *179*, 1110–1118. [CrossRef]
26. Azevedo, M.S.; Allély, C.; Ogle, K.; Volovitch, P. Corrosion mechanisms of Zn (Mg, Al) coated steel: 2. The effect of Mg and Al alloying on the formation and properties of corrosion products in different electrolytes. *Corros. Sci.* **2015**, *90*, 482–490. [CrossRef]
27. Wint, N.; Malla, A.D.; Cooze, N.; Savill, T.; Mehraban, S.; Dunlop, T.; Sullivan, J.H.; Penney, D.; Williams, G.; McMurray, H.N. The ability of Mg_2Ge crystals to behave as 'smart release'inhibitors of the aqueous corrosion of Zn-Al-Mg alloys. *Corros. Sci.* **2021**, *179*, 109091. [CrossRef]
28. Hausbrand, R.; Stratmann, M.; Rohwerder, M. Corrosion of zinc–magnesium coatings: Mechanism of paint delamination. *Corros. Sci.* **2009**, *51*, 2107–2114. [CrossRef]
29. Byun, J.M.; You, J.M.; Kim, D.K.; Kim, T.Y.; Jeong, W.S.; Kim, Y.D. Corrosion Behavior of Mg_2Zn_{11} and $MgZn_2$ Single Phases. *Korean J. Met. Mater.* **2013**, *51*, 413–419. [CrossRef]

30. Voith, M.; Mardare, A.I.; Hassel, A.W. Synthesis and characterization of Al–M g–Z n thin film alloys co-deposited from vapour phase. *Phys. Status Solidi A* **2013**, *210*, 1000–1005. [CrossRef]
31. Volovitch, P.; Allely, C.; Ogle, K. Understanding corrosion via corrosion product characterization: I. Case Study of the Role of Mg Alloying in Zn–Mg coating on steel. *Corros. Sci.* **2009**, *51*, 1251–1262.
32. Conway, B.E.; Kannangara, D. Zinc oxidation and redeposition processes in aqueous alkali and carbonate solutions: II. Distinct-inction between Dissolution and Oxide Film Formation Processes. *J. Electrochem. Soc.* **1987**, *134*, 906.
33. Ishikawa, T.; Matsumoto, K.; Yasukawa, A.; Kandori, K.; Nakayama, T.; Tsubota, T. Influence of metal ions on the formation of artificial zinc rusts. *Corros. Sci.* **2004**, *46*, 329–342. [CrossRef]
34. Anjum, M.J.; Zhao, J.; Ali, H.; Tabish, M.; Murtaza, H.; Yasin, G.; Malik, M.U.; Khan, W.Q. A review on self-healing coatings applied to Mg alloys and their electrochemical evaluation techniques. *Int. J. Electrochem. Sci.* **2020**, *15*, 3040–3053. [CrossRef]
35. Vu, A.Q.; Vuillemin, B.; Oltra, R.; Allély, C. Cut-edge corrosion of a Zn–55Al-coated steel: A comparison between sulphate and chloride solutions. *Corros. Sci.* **2011**, *53*, 3016–3025. [CrossRef]